Check for updates

ARTICLE   **OPEN**

Electrochemical corrosion of multiphase stainless steel-based alloy nuclear waste forms

Vineeth Kumar Gattu [1 ✉], William L. Ebert[1], J. E. Indacochea[1], Terry A. Cruse[1] and Jeffrey A. Fortner [1]

The electrochemical corrosion behaviors of two multiphase alloys representing waste forms made with 316 L stainless steel and different amounts of surrogate metallic fuel wastes were measured and related to the microstructures. Potentiodynamic (PD) scans were performed in an acid brine solution and the corroded surfaces were characterized with scanning electron microscopy (SEM) to compare the electrochemical responses to the corrosion of specific phases. PD scans for the two multiphase alloys, 316 L stainless steel, and pure palladium were compared to understand the complex corrosion behavior of these multiphase alloys also recently classified as multi principle element alloys (MPEAs) and to determine the effects of alloying elements and noble metals present in constituent phases on the corrosion behavior.

INTRODUCTION

Deep geological disposal systems are being designed in several countries with multiple barriers to mitigate transport of dose-generating radionuclides outside the repository boundary for several hundred thousands of years[1]. These barriers include the host geology, backfill materials (such as crushed bentonite), an engineered barrier system (EBS) that may consist of metallic and concrete barriers, carbon steel overpacks, corrosion-resistant waste packages and canisters, and durable waste forms that provide the initial containment barrier[2]. The primary pathway for radionuclide release is by seepage water penetrating these barriers to contact and degrade the waste form. The released radionuclides can migrate away from the EBS by dispersive and advective groundwater transport. Therefore, waste forms are being designed to resist corrosion under the range of seepage water compositions that could occur in a breached waste package during the regulated service life of a disposal facility. The chemistries of those seepage waters will be affected by the groundwater composition, container corrosion products, radiolysis, and the range of corrosion products generated during the degradation of backfill materials, neighboring waste forms, and the waste form itself. In the United States, generic disposal systems constructed in granitic, argillite, and salt formations are being evaluated for the possible co-disposal of glass, glass/ceramic, and metal waste forms with directly-disposed spent fuel. This requires that the degradation behaviors in a wide range of possible seepage water compositions be considered during the design of the waste forms (and other EBS components) and in models being developed to represent degradation of those materials in simulations conducted to ensure dose limits will be met.

Stainless steel-based waste forms were developed at Argonne National Laboratory (ANL) in the 1990s to immobilize high-level radioactive wastes from the electrometallurgical treatment of used sodium-bonded nuclear fuel[3–5]. These metal waste forms are produced by alloying residual metallic fuel wastes and steel cladding hulls recovered from the electrorefiner with small amounts of trim metal additions (e.g., Cr, Mo, and Ni) to produce a multiphase alloy composed of physically, chemically, and radiologically durable intermetallic and solid solution phases that contain the radionuclides. Waste forms can be produced by directly melting wastes at temperatures near 1650 °C because waste constituents having high melting temperatures dissolve into molten steel at temperatures well below their melting points.

Initial metallurgical analyses and corrosion tests showed the prototype alloys effectively accommodated and retained radionuclides[6–13] and were used to support preliminary assessments of waste form performance in a disposal facility[14–17]. The successful production of full-scale metal waste forms from processing wastes generated during electrometallurgical treatment of steel-clad sodium-bonded fuel from the Experimental Breeder Reactor-II (EBR-II) has been demonstrated at the Idaho National Laboratory (INL)[18].

Other metallic waste forms are being developed to immobilize waste stream compositions anticipated to be generated during advanced fuel cycle operations with spent reactor fuels in HT9 steel and Zircaloy cladding[19–21]. Key aspects of waste form development include (1) the capacity to accommodate waste constituents in durable phases, (2) reliable production methods that generate waste form products having consistent properties, and (3) confidence that the waste forms will meet regulatory requirements during handling, storage, transport, and permanent disposal. The major performance requirement for metal waste forms is to maintain sufficient corrosion resistance that the disposal system will remain compliant with regulations throughout its service life.

Multiphase alloys, recently described as multi principle element alloys (MPEAs) are being developed for use in many engineering applications[22]. The mechanistic rationalization of the corrosion of MPEAs will depend on the metallurgical phases that are formed during melting, their chemical compositions, and relative amounts of the phases exposed to the environment. In addition, the corrosion of multiphase alloy waste forms depends on the relative amounts of cladding, fuel wastes, and added trim metals used to produce it. The corrosion behavior of different radionuclide host phases in multiphase alloy nuclear waste form will be affected by galvanically coupled corrosion behaviors of each phase. The oxidation of radionuclides in a host phase may be limited by

---

[1]Chemical and Fuel Cycle Technologies Division, Argonne National Laboratory, Lemont, IL, USA. ✉email: gvk@anl.gov
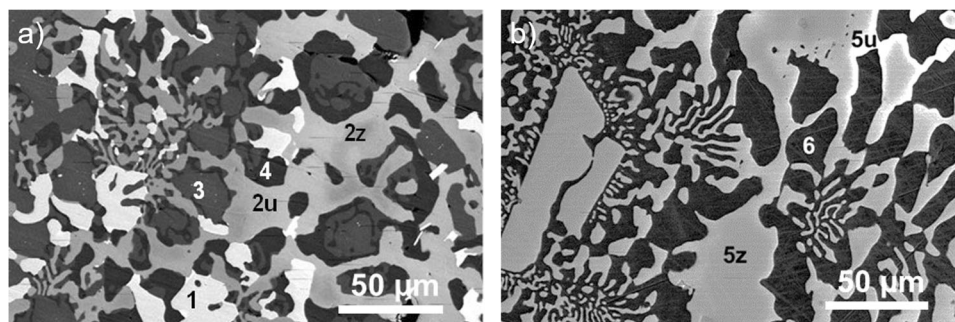
Fig. 1 SEM micrographs of multiphase alloy nuclear waste forms. Showing results for **a** RAW-2 and **b** RAW-4. The scale bar on the images is 50 μm.

Table 1. Compositions of constituent phases in RAW-2, in at %[a].

Phase No.[a]	Phase ID	Fe	Cr	Ni	Mo	Mn	Si
1 (15)	$ZrPd_2$	3.3 ± 1.0	0.5 ± 0.4	12 ± 4	0.0	0.5 ± 0.4	0.0
2u (17)	$ZrFe_2$-u	31 ± 4	3.3 ± 0.2	19 ± 4	0.2 ± 0.4	1.3 ± 0.4	2.1 ± 0.8
2z (13)	$ZrFe_2$-z	35 ± 6	4.5 ± 1.6	16 ± 24	0.4 ± 0.6	1.4 ± 0.6	2.7 ± 0.8
3 (16)	γ-Austenite	62 ± 4	17 ± 2	7.8 ± 1.0	2.0 ± 1.0	1.6 ± 0.4	0.3 ± 0.6
4 (16)	α-Ferrite	52 ± 4	24 ± 2	4.2 ± 0.8	5.7 ± 1.0	1.5 ± 0.6	0.4 ± 0.2

Phase No.[b]	Phase ID	Zr	U	Tc	Ru	Pd	Rh
1 (15)	$ZrPd_2$	22 ± 2	1.7 ± 1.8	0.0	1.6 ± 1.4	55 ± 4	4.0 ± 1.8
2u (17)	$ZrFe_2$-u	20 ± 4	4 ± 2	0.1 ± 0.2	10 ± 4	4.3 ± 1.0	2.8 ± 0.6
2z (13)	$ZrFe_2$-z	23 ± 2	1.5 ± 1.4	0.2 ± 0.6	11 ± 4	4.0 ± 0.6	2.6 ± 0.8
3 (16)	γ-Austenite	0.07 ± 0.16	0.06 ± 0.12	2.5 ± 0.6	5.9 ± 1.8	0.5 ± 0.2	0.5 ± 0.4
4 (16)	α-Ferrite	0.13 ± 0.08	0.05 ± 0.06	5.1 ± 1.8	6.1 ± 1.6	0.3 ± 0.4	0.3 ± 0.4

[a]Values presented as mean ± 2 s for measured domains.
[b]Values in parentheses give number of separate domains of the phase that were analyzed.

passivation of that phase and their release may be further restricted by the solubilities of radionuclide-bearing oxide phases that form.

In this study, two surrogate multiphase alloy nuclear waste forms defined as reference alloy waste (RAW) forms were cast by adding different amounts of Zr, Mo, U, and noble metals to Type 316 L stainless steel. The objective was to assess the effects of microstructure, elemental compositions (primarily U, Tc, and noble metals), and waste loading on the corrosion behavior to assist in the formulation of alloy waste forms for specific waste stream compositions that are durable under the range of environmental conditions for possible disposal systems.

RESULTS AND DISCUSSION
Metallurgical characterization
The microstructures of freshly polished RAW-2 and RAW-4 materials are shown in Fig. 1 as SEM BSE images of representative areas of the cross-sectioned ingots. The RAW-2 alloy (Fig. 1a) has a complex microstructure composed of four distinct phases (identified as Phases 1–4) present with coarse and blocky proeutectic morphologies that are mixed with small regions of the same phases having fine eutectic microstructures. The RAW-4 alloy (Fig. 1b) is composed of similar amounts of two phases (identified as Phases 5 and 6) that occur with blocky morphologies intermingled with domains of the same phases having a fine eutectic lamellar microstructure. As discussed below, the contrast differences seen in some regions of Phase 2 in RAW-2 (brighter regions labeled 2 u and darker regions 2z) and some regions of Phase 5 in RAW-4 (brighter regions labeled 5 u and darker regions 5z) reflect compositional differences within the same phases.

The compositions of the constituent phases in RAW-2 and RAW-4 were measured at several locations on the polished cross sections. Averages of the elemental concentrations measured by EDS analyses of between ten and twenty domains of each phase in alloys RAW-2 and RAW-4 are summarized in Tables 1, 2, respectively. The four phases comprising alloy RAW-2 are a $ZrPd_2$ intermetallic (Phase 1), $ZrFe_2$ Laves-type intermetallics (Phase 2) with compositionally distinct regions labeled 2 u and 2z, γ-austenite (Phase 3), and α-ferrite (Phase 4). Alloy RAW-4 is composed of two phases: a proeutectic $ZrFe_2$ phase (Phase 5) and α-ferrite (Phase 6). The $ZrFe_2$ phase was identified previously as a $Zr(Fe, Ni, Cr)_{2+x}$ Laves-type intermetallic[11,12] and has two compositionally distinct regions labeled 5 u and 5z. These are present as blocky domains and eutectic $ZrFe_2$ + α-ferrite. Close inspection of Phase 6 (Fig. 1b) reveals blade-like features that are common to fast-cooled ferrous alloys.

The $ZrFe_2$ phases in both materials have high Ni contents and low Cr and Mo contents. The U:Zr ratios vary throughout the Phase 5 domains. For convenience, regions of the $ZrFe_2$ intermetallic with high U:Zr ratios are referred to as $ZrFe_2$-u and regions with lower ratios are referred to as $ZrFe_2$-z. The noble metals are distributed between different phases: $ZrPd_2$ intermetallic is the primary host phase for Pd and Rh in RAW-2, whereas Ru reports primarily to the $ZrFe_2$ phases in both materials with only small amounts measured in the other phases. The Tc in each material reports to both the ferritic and austenitic phases, but prefers the

Table 2. Compositions of constituent phases in RAW-4, in at %[a].

Phase No.[a]	Phase ID	Fe	Cr	Ni	Mo	Mn	Si
5u (9)	ZrFe$_2$-u	46 ± 4	2.5 ± 1.2	22 ± 4	0.1 ± 0.4	0.7 ± 0.8	1.4 ± 1.0
5z (20)	ZrFe$_2$-z	51 ± 4	5.1 ± 1.6	17 ± 4	0.1 ± 0.4	1.1 ± 0.8	1.8 ± 1.6
6 (20)	α-Ferrite	70 ± 2	24 ± 1.4	2.1 ± 1.4	0.9 ± 0.4	1.2 ± 1.0	0.3 ± 0.4

Phase No.[b]	Phase ID	Zr	U	Tc	Ru	Pd	Rh
5u (9)	ZrFe$_2$-u	13 ± 6	10 ± 6	0.0	0.7 ± 1.6	2.0 ± 1.6	1.2 ± 1.2
5z (20)	ZrFe$_2$-z	21 ± 2	2 ± 2	0.0	0.1 ± 0.4	1.2 ± 1.2	0.3 ± 1.0
6 (20)	α-Ferrite	0.07 ± 0.18	0.02 ± 0.08	0.9 ± 0.4	0.3 ± 0.4	0.2 ± 0.4	0.2 ± 0.4

[a]Values presented as mean ± 2 s for measured domains.
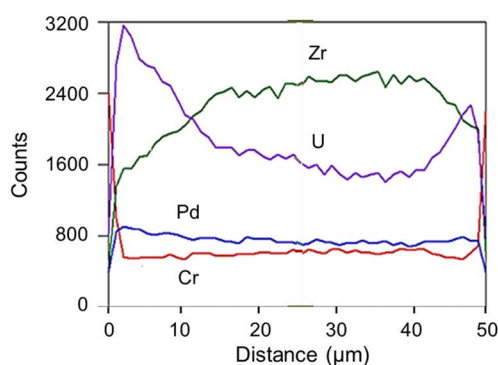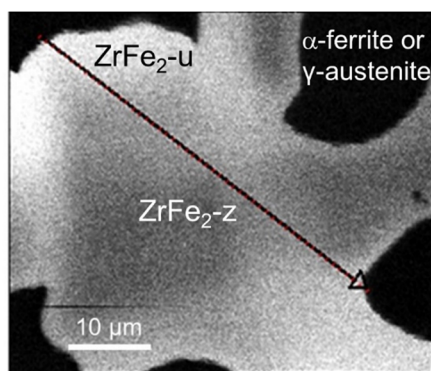[b]Values in parentheses give number of separate domains of the phase that were analyzed.

Fig. 2 EDS line profile measures the relative amounts of Zr and U in the FeZr$_2$ phase in the multiphase alloy nuclear waste form. Showing results for RAW-2. The scale bar on the left image 10 µm.

Table 3. Estimated area fraction amounts of the phases in the three alloys, %.

Alloy	Austenite	Ferrite	ZrFe$_2$-z	ZrFe$_2$-u	ZrPd$_2$
316 L	100	0	–	–	–
RAW-4	0	50	48	2	–
RAW-2	33	30	20	10	7

Fig. 3 PD scans in air saturated acidic NaCl solution at room temperature. Showing results for RAW-2, RAW-4, 316L SS, and Pd materials.

body-center cubic (bcc) structure of the ferritic phases. The ferrite formed in RAW-4 has lower Mo and noble metal contents than the ferrite formed in RAW-2 because only the Mo provided by 316 L stainless steel was present in RAW-4. The ZrPd$_2$ and ZrFe$_2$ intermetallics both host U (see also[23]), which prefers phases with face-centered cubic (fcc) structures. The distribution of Nb in RAW-4 was not measured in this study, but previous analyses of similar materials indicate Nb reports to the ZrFe$_2$ intermetallic[9].

The EDS spot analyses of the phases in Fig. 1 show that U is enriched in the outer regions of the ZrFe$_2$ phases in both RAW-2 and RAW-4. The results of an EDS line profile across a typical ZrFe$_2$ domain in RAW-2 in the direction of the arrow are shown in Fig. 2. The black regions in the SEM image are either ferrite or austenite, the brightest regions are ZrFe$_2$-u, and the darker interior regions are ZrFe$_2$-z. The line profiles on the right-hand side of Fig. 2 show smooth changes in the U and Zr concentrations across the phase that are consistent with the replacement of Zr by U in the structure. The Pd and Cr contents are uniform across the phase and not correlated with the U or Zr concentrations.

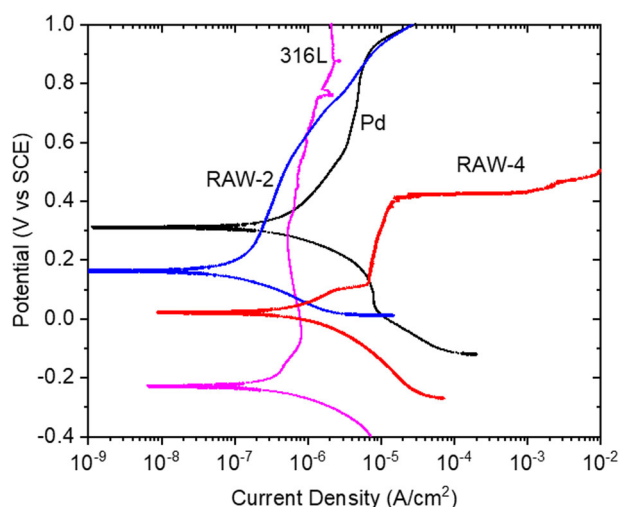Differences in the relative amounts of U and Zr in ZrFe$_2$-u and ZrFe$_2$-z regions are probably due to kinetic limits on homogenization during the rapid solidification of the intermetallic when the RAW-2 alloy was cast. For U:Zr ratios similar to those in RAW-2 and RAW-4, the U-Zr binary phase diagram[23] indicates that the α-Zr phase will form with a low U content from a cooling γ-U and β-Zr intermetallic at about 650 °C and that the Laves phase will form at 610 °C. This suggests the ZrFe$_2$-z domains formed first and displaced most of the U to the perimeter as the ingots of RAW-2 and RAW-4 cooled.
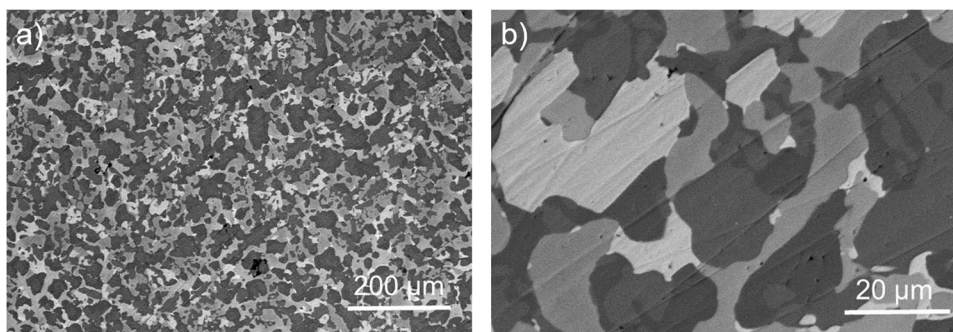
Fig. 4 SEM micrographs after the PD scan in acidic brine solution. Showing results of RAW-2 **a** low and **b** high magnification. The scale bar on the left image is 200 µm and the right image is 20 µm.
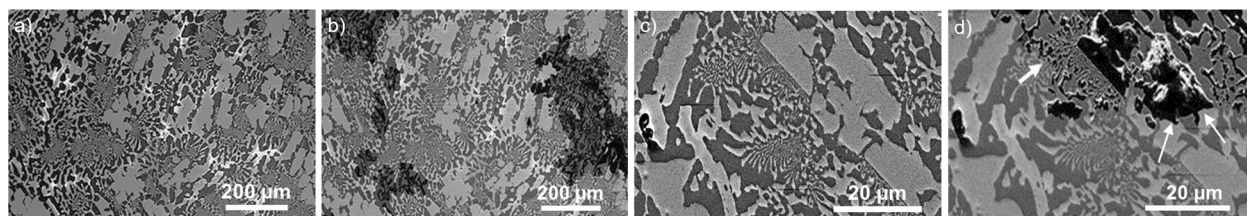

Fig. 5 SEM micrographs of RAW-4 after the PD scan in acidic brine solution. Showing results for low magnification images **a** before and **b** after the PD scan and high magnification images **c** before and **d** after the PD scan; arrows point to the localized corrosion. The scale bars on the lower magnification images is 200 µm and for the higher magnification images is 20 µm.

The compositions measured at low magnification in several locations of the cross sections were in good agreement with the batched compositions. We analyzed several SEM backscattered electron images of ~0.01 mm^2 areas of the cross-sections by using FoveaPro 4.0 (Reindeer Graphics) with Adobe Photoshop to determine the relative areas of the constituent phases. The results are summarized in Table 3. The relative areas of α-ferrite, $ZrFe_2$-z, and $ZrFe_2$-u phases in RAW-4 were measured to be about 50:48:2. Analysis of the RAW-2 ingot indicated the relative areas of γ-austenite, α-ferrite, $ZrFe_2$, and $ZrPd_2$ were about 33:30:30:7. The separate amounts of the $ZrFe_2$-u and $ZrFe_2$-z phases in RAW-2 could not be differentiated by using the SEM images, but area analyses of elemental EDS maps indicated there was about 20% $ZrFe_2$-z and 10% $ZrFe_2$-u. The volume fractions in the ingot are assumed to be the same as the measured area fractions. These provide the area fractions across the ingot, but the fractions on the smaller scale of each electrode surface will differ and affect the electrochemical test responses.

Potentiodynamic scans

Representative PD scans for freshly polished (and cathodically cleaned) surfaces of RAW-2, RAW-4, palladium (Pd) and 316 L stainless steel electrodes in the acidic NaCl solution are shown in Fig. 3. The values of E_{CORR} for RAW-2 and RAW-4 depend on the relative surfaces areas of the constituent phases that are exposed after each polishing. The PD response is due to simultaneous and coupled corrosion of several phases that must be taken into account in the interpretation. The PD scan for Pd is included to highlight the effects of noble metals and this will be discussed in more detail in Section 2.5. The measured E_{CORR} values are 0.18 V_{SCE} for RAW-2, 0.02 V_{SCE} for RAW-4, 0.31 V_{SCE} for Pd, and −0.23 V_{SCE} for 316 L. RAW-2 shows a more noble E_{CORR} and lower anodic current densities than RAW-4 and 316 L SS at voltages up to 0.62 V_{SCE}. Both RAW-2 and 316 L stainless steel show extended passive regions for voltages up to 1.0 V_{SCE}, but the current densities for 316 L stainless steel in the passive region increase only slightly at voltages above 0.62 V_{SCE} compared to the continuous increase seen for RAW-2. The PD scan with RAW-4 shows a sharp bend at

0.1 V_{SCE} which is most likely caused by a dominant anodic reaction of a more actively corroding phase. The PD scan of RAW-4 has a narrow passive region with current densities more than one order of magnitude higher than those measured for 316 L stainless steel and two orders of magnitude higher than those measured for RAW-2. The PD scan with RAW-4 shows breakdown behavior at potentials above about 0.42 V_{SCE} due to possible localized corrosion of a relatively active phase in the microstructure. These results show that RAW-2 and 316 L stainless steel are more stable alloys than RAW-4 with more extensive passive regions under these conditions.

Microstructural assessments following PD scan

Differences in the PD scan responses of the alloys shown in Fig. 3 are attributed, in part, to the effects of the microstructure and phase compositions on the corrosion behavior. Materials RAW-2 and RAW-4 have different microstructures, with different area fractions and compositions of the constituent phases: ferrite is the dominant iron-bearing phase in RAW-4 and no austenite was detected, whereas similar amounts of ferrite and austenite formed in RAW-2. 316 L is a single phase austenitic stainless steel. The three alloys are further distinguished by the different amounts of noble metals: RAW-2 contains significant amounts, RAW-4 contains a small amount, and 316 L contains no noble metals. The electrode surfaces were examined after the PD scans to determine which phases corroded. The electrode surfaces of RAW-2 were identical before and after the PD scan which indicates extremely low corrosion. The SEM images of the RAW-2 electrode surface after the PD scan are shown in Fig. 4. However, significant localized corrosion occurred on the RAW-4 electrode. Figure 5 shows the microstructures of two separate regions of the RAW-4 electrode prior to and after the PD scan. Figure 5a, b are relatively low magnification images that show corrosion occurred in localized regions. Figure 5c, d are higher magnification images taken at a different location that show which phases corroded. Figure 5c displays the microstructure prior to the PD scan showing regions of the large proeutectic $ZrFe_2$ phase (light contrast) and eutectic microstructure consisting of fine $ZrFe_2$ intermetallic

Table 4. Cr, Mo, and Ni contents of the austenite and ferrite phases in the three alloys, in at%.

Alloy	Phase	Fe	Cr	Ni	Mo	Mn	Si
316 L SS[a]	γ-Austenite	71	18	8	2–3	1.0	–
RAW-2	γ-Austenite	62 ± 4	17 ± 2	7.8 ± 1.0	2.0 ± 1.0	1.6 ± 0.4	0.3 ± 0.6
	α-Ferrite	52 ± 4	24 ± 2	4.2 ± 0.8	5.7 ± 1.0	1.5 ± 0.6	0.4 ± 0.2
RAW-4	α-Ferrite	70 ± 2	24 ± 1.4	2.1 ± 1.4	0.9 ± 0.4	1.2 ± 1.0	0.3 ± 0.4

[a]Nominal values.

phases intermingled with ferrite (the phase with darker contrast). Figure 5d shows the microstructure after PD that indicates preferential galvanic corrosion of proeutectic and eutectic $ZrFe_2$ intermetallic phase occurred in areas marked by the white arrows, whereas no corrosion is detected in the neighboring regions of α-ferrite.

Two aspects are considered in assessing the corrosion behavior of these multiphase alloys: differences in the relative amounts and compositions of austenite and ferrite phases and the abundance of noble metal-bearing phases. The next two sections describe these factors.

Effects of austenite and ferrite

The PD scan of 316 L stainless steel shown in Fig. 3 is typical for this alloy in an aqueous chloride acidic environment[24]. The passive region at low potentials is attributed to the formation of Cr_2O_3 and the extended passive region at high potentials is attributed to the formation of $NiMoO_4$[25]. The high chromium, nickel, and molybdenum contents of 316 L stainless steel support formation of these protective oxides. Table 4 summarizes the measured compositions of the iron-bearing phases in the three alloys to facilitate comparisons of the PD scans. The corrosion resistance of RAW-4 is lower than that of 316 L stainless steel which is likely related to the composition of the α-ferrite that comprises ~50 vol% of RAW-4. The Cr content is sufficient to support passivation of ferrite at low potentials, but the Ni and Mo contents are not sufficient to passivate ferrite at high potentials. The PD scan in Fig. 3 for RAW-4 shows a breakdown behavior at potentials above 0.42 V_{SCE}, which exceeds the stability range of Cr_2O_3. However, it was observed in SEM that α-ferrite did not corrode but the ZrFe2 intermetallic corroded preferentially (see Fig. 5d). This is most likely because the $ZrFe_2$ intermetallic do not contain sufficient levels of Cr to form a passivating Cr_2O_3 layer. In addition, despite the high Ni content (17–22 at%) in $ZrFe_2$ intermetallic, the trace amount of Mo is not sufficient to form a $NiMoO_4$ layer. Consequently, the $ZrFe_2$ phase exhibits poor pitting resistance, which probably leads to active dissolution of the phase. Furthermore, compositional differences between the α-ferrite and $ZrFe_2$ intermetallic leads to the galvanic coupling and preferential corrosion of the latter phase.

The lower current densities and expanded passive region indicate RAW-2 is more corrosion resistant than RAW-4. This can directly be attributed to the high amount of γ-austenite in RAW-2 (~33 vol%), which has the same composition as austenite in 316 L SS. In addition, the α-ferrite formed in RAW-2 is probably more durable than the α-ferrite formed in RAW-4 because it contains twice the amount of Ni, more Mo, and the same amount of Cr (see Table 4). Both Ni and Mo are known to improve passivity in austenitic stainless steels and extend the passivity range[25–27].

Although the current densities in the PD scan of RAW-2 were significantly lower than those in the PD scan of RAW-4 due to the presence of γ-austenite and more durable α-ferrite, extensive corrosion of the $ZrFe_2$ intermetallics occurred in RAW-4 but not in RAW-2. It appears that the presence of $ZrPd_2$ and the higher noble metal contents in the other phases (see Tables 1 and 2) improves the corrosion resistance of RAW-2 beyond that of 316 L stainless

steel for voltages up to 0.62 V_{SCE}. The influence of the noble metals in the corrosion performance of these alloys is described in the next section.

Effects of noble metals

PD scans corresponding to 316 L SS, RAW-2, RAW-4, and pure palladium (Pd) are shown in Fig. 3. The PD scan for Pd in acid brine solution is included to differentiate the effects of noble metals from other compositional effects. The E_{CORR} value measured in the PD scan of 316 L SS is the lowest, followed by RAW-4 that contains ~3.0 wt% noble metals, and RAW-2 that has ~20.9 wt% noble metals. The E_{CORR} value measured for pure palladium (~ 0.3 V_{SCE}) is higher than values measured for the three alloys, which indicates that E_{CORR} values increase with increases in the noble metal content. The anodic current densities measured in the PD scan for RAW-2 are lower than 316 L SS and palladium for voltages up to about 0.62 V_{SCE}. Higher current densities were measured in the PD scan for palladium than in the PD scan with RAW-2 until the anodic curves converged above about 0.85 V_{SCE}; this suggests the oxidation behavior of RAW-2 became controlled by the electrochemical activities of the noble metals.

The presence of noble metals affects the corrosion behaviors of the alloy matrix and neighboring phases through electrochemical effects. The noble metals catalyze hydrogen generation reactions (represented by the cathodic half-reaction in Eq. 1) that couple with anodic reactions (represented by the half-reaction for metallic element in Eq. 2). The rate of hydrogen evolution for reactions catalyzed by noble metals on the alloy surface is about five orders of magnitude higher than the rates of reactions catalyzed by other metals[28–31].

$$2H^+ + 2e^- \rightarrow H_2 \tag{1}$$

$$M \rightarrow M^{n+} + ne^- \tag{2}$$

The generation of H_2 probably provides the dominant cathodic current measured in the PD scans with RAW-2 and RAW-4 and enobles E_{CORR} compared to 316 L SS. The higher cathodic currents in the PD scans with RAW-4, RAW-2, and Pd at potentials below their respective E_{CORR} are consistent with higher H_2 generation rates occurring on surfaces with higher noble metal contents (about 3 wt% in RAW-4, 20.9 wt% in RAW-2, and 100 wt% in Pd). The $ZrFe_2$ intermetallic phases in RAW-2 and RAW-4 have similar Mo and Cr contents, but the corrosion resistance of RAW-2 is higher than RAW-4. This can be attributed to the higher noble metal contents of constituent phases in RAW-2 compared with RAW-4, primarily Pd and Ru (see Table 1).

Corrosion of multiphase alloy waste forms

In summary, the effects of Zr, Mo, noble metals, and radionuclides (U and Tc) on the microstructure and corrosion performance of two 316 L SS-based alloy waste forms, RAW-2 and RAW-4, were evaluated. The microstructure of RAW-4 exhibited ferrite and intermetallic FeZr2 phases. RAW-2 comprised of the same phases but it also had austenite and $ZrPd_2$ intermetallic phases. The ferrite in RAW-2 contained the same amount of Cr but higher levels of Ni,

Table 5. Approximate as-batched alloy compositions, in wt%.

	Fuel Cladding Hulls[a]						Metallic Fuel Waste							
	Fe	Cr	Ni	Mo	Mn	Si	Zr	U	Tc	Mo	Ru	Pd	Rh	Nb
RAW-2	39	11	7.4	1.4	1.0	0.3	9.7	2.4	3.7	3.2	11.3	7.6	2.0	—
RAW-4	51	14	9.7	1.7	1.2	0.4	15	2	1	—	1	1	1	1

[a]Nuclear fuel rod outer jacket; 316 L SS composition: 71.5Fe–16–18Cr–8Ni–2.5Mo–0.2Mn.
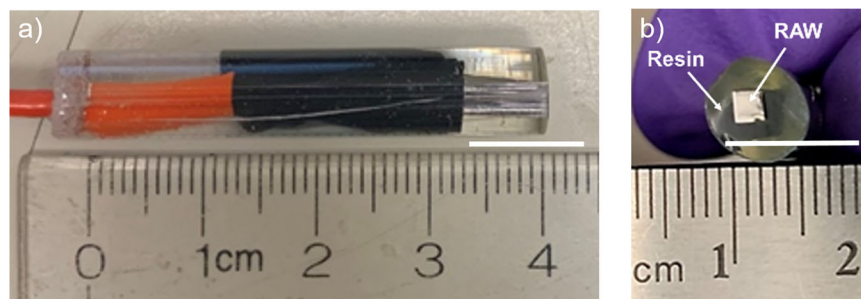
Fig. 6 Photos of of the working electrode. Showing results for **a** side and **b** cross-section end. The scale bar on both the images is 1 cm.

Mo and noble metals than RAW-4. The intermetallic phases in RAW-2 also show higher amounts of noble metals than RAW-4.

Potentiodynamic scans showed the impacts of different phase compositions and microstructures on the corrosion behaviors of these multiphase alloy waste forms. The corrosion behaviors were sensitive to the amounts of ferrite and austenite and the ferrite compositions in each waste form. The responses were also sensitive to the amounts of noble metals in the constituent phases and probably the formation of a $ZrPd_2$ intermetallic. The relative effects of passivating elements and noble metals were distinguished by comparisons with the PD responses of 316 L and pure palladium. The differences due to compositions of Fe-bearing phases and are consistent with the amounts of passivating elements Cr, Ni, and Mo in the constituent phases. Furthermore, corrosion obeserved in RAW-4 was due to the compositional differences between the α-ferrite and $ZrFe_2$ intermetallic phases which led to the galvanic coupling and preferential corrosion of the latter phase. The effect of the noble metals is attributed to catalyzed generation of a H_2-rich microenvironment. The H_2 generation can provide the dominant cathodic current and increase (enoble) E_{CORR}. These results also show that ennoblement of E_{CORR} is not beneficial to the corrosion behavior of the alloy if sufficient amounts of passivating elements are not present in the constituent phases or if galvanic couples are generated due to the presence of phases with different compositions in the microstructure.

This study also shows that the corrosion behavior of multiphase alloys, described as MPEAs, is determined by the concentrations of alloying elements in the constituent phases and the abundance of those phases in the microstructure. Therefore, both the metallurgical and electrochemical responses of individual phase components must be considered to understand their overall corrosion behavior.

METHODS
Alloy waste form fabrication
Laboratory-scale ingots of RAW-2 and RAW-4 materials were produced at INL by melting mixtures of AISI Type 316 L stainless steel chips (SRM 160b) to represent fuel cladding with Zr wire and metal powders representing fuel waste in an ultra-pure argon atmosphere at approximately 1650 °C[32] for about 2 h. The as-batched elemental compositions of the alloys are provided in Table 5. Alloy RAW-2 was formulated with a similar Zr/Fe ratio

as RAW-4 to generate similar intermetallic phases but with higher concentrations of noble metals to represent a higher waste loading.

Metallurgical characterization
A polished cross section of each ingot was prepared to characterize the microstructure and measure the compositions of the constituent phases by using a scanning electron microscope (SEM) with associated energy-dispersive X-ray emission spectrometer (EDS). Microscopy was performed using both secondary and backscattered electron (BSE) imaging to highlight morphological and compositional differences, respectively. The uniformity of the microstructure and phase compositions in each cross section was assessed by areal analyses of broad regions, spot analyses of each phases at several locations throughout the cross-section, and line profiles spanning phase domains and crossing phase boundaries.

Electrochemical measurements
Several specimens were cut from the RAW-2 and RAW-4 ingots as parallelepipeds with dimensions of about $1 \times 2 \times 15$ mm^3 for use in the electrochemical tests. Each test specimen was fixed in acrylic resin to produce an electrode about 6 mm in diameter and 5 cm long. The alloy area exposed at the end of the electrode was approximately 2 mm^2 (see Fig. 6). The surface area of alloy exposed in each electrode was measured by using the SEM to normalize the currents measured during the electrochemical tests as current densities for direct comparisons of responses from different electrodes and different alloys. Similar electrodes were made from small sections cut from a commercial 316 L stainless steel rod and a pure palladium rod.

Potentiodynamic (PD) scans were conducted at room temperature in approximately 15 mL of an air-saturated acidic NaCl solution (0.1 mmolal $H_2SO_4 + 10$ mmolal NaCl adjusted to pH 4). The solution represents seepage water that has interacted with bentonite backfill (which contributes chloride) and was acidified due to corrosion of the waste package and radiolysis. Although the measured corrosion potential (E_{CORR}) in the PD scan provides an indication of the corrosion behavior, corrosion at potentials lower and higher than E_{CORR} represent possible disposal conditions of interest. We need to understand the corrosion behavior over a wide range of potentials, not only at E_{CORR} measured in these tests. The shapes of anodic and cathodic legs provide initial insights into the corrosion behavior to guide follow-on tests.

An electrode made from a specimen of RAW-2, RAW-4, 316 L stainless steel, or palladium was used as the working electrode in a cell with a KCl-saturated calomel reference electrode (SCE) and a graphite counter electrode. Graphite was used to minimize the contribution of the cathodic reactions occurring on the counter electrode and highlight the effects of noble metals on the alloy surface. Unless stated otherwise, voltages are reported relative to the SCE and indicated as V_{SCE}. Photographs of an

electrode and the experimental apparatus are shown in Fig. 6. The electrochemical tests were performed using a computer-controlled potentiostat (Princeton Applied Research VersaSTAT 4). Commercial software (Princeton Applied Research VersaStudio) was used to analyze the data and generate standard plots. The PD scans were used to characterize the corrosion behaviors of the polished surfaces by scanning the potential from -0.25 V vs OCP to $+1.60$ V_{SCE} at a scan rate of 0.16 mV s^-1. These scans were conducted for ranges that exceed redox conditions anticipated for disposal facilities to augment the mechanistic understanding of the degradation process and promote SEM-detectable corrosion of the least durable phase during the scan. Significant volumes of solutions with redox potentials higher than 0.6 V_{SCE} may not be physically achievable in a disposal system, but small amounts could occur in localized microenvironments.

DATA AVAILABILITY

The data that support the findings of this study are available from the corresponding author upon reasonable request.

REFERENCES

1. International Atomic Energy Agency, *Planning and Design Considerations for Geological Repository Programmes of Radioactive Waste*, Vienna, Austria, IAEA-TECDOC-1755 (2014).
2. Féron, D., Crusset, D. & Gras, J. M. Corrosion issues in nuclear waste disposal. *J. Nucl. Mater.* **379**, 16–23 (2008).
3. Abraham, D. P., Keiser, D. D. & McDeavitt, S. M. Metal waste forms from treatment of EBR-II spent fuel. *Proceedings of the International Conference on Decommissioning and Decontamination and on Nuclear and Hazardous Waste Management Spectrum*. Denver, Colorado, pp 783–789 (1998).
4. McDeavitt, S. M., Abraham, D. P., Keiser, D. D. & Park, J. Y. Alloy waste forms for metal fission products and actinides isolated by spent nuclear fuel treatment. *Proceedings of the Second International Symposium on Extraction and Processing for the Treatment and Minimization of Wastes*. Scottsdale, Arizona, pp. 177–189 (1996).
5. Janney, D. E. & Keiser, D. D. Jr Actinides in metallic waste from electrometallurgical treatment of spent nuclear fuel. *JOM* **55**, 59–60 (2003).
6. McDeavitt, S. M., Abraham, D. P. & Park, J. Y. Evaluation of stainless steel-zirconium alloys as high-level nuclear waste forms. *J. Nucl. Mater.* **257**, 21–34 (1998).
7. Janney, D. E. Host phases for actinides in simulated metallic waste forms. *J. Nucl. Mater.* **323**, 81–92 (2003).
8. Keiser, D. D. Jr., Abraham, D. P. & Richardson, J. W. Jr Influence of technetium on the microstructure of a stainless steel-zirconium alloy. *J. Nucl. Mater.* **277**, 333–338 (2000).
9. Abraham, D. P. & Dietz, N. L. Role of laves intermetallics in nuclear waste disposal. *Mater. Sci. Eng. A.* **A329–331**, 610–615 (2002).
10. Abraham, D. P., Richardson, J. W. Jr. & McDeavitt, S. M. Laves intermetallics in stainless steel-zirconium alloys. *Mater. Sci. Eng. A* **A239–240**, 658–664 (1997).
11. Abraham, D. P., Richardson, D. P. J. W. Jr. & McDeavitt., S. M. Formation of the $Fe_{23}Zr_6$ phase in an Fe-Zr alloy. *Scr. Mater.* **37**, 239–244 (1997).
12. Abraham, D. P., McDeavitt, S. M. & Park., J. Y. Microstructure and phase identification in type 304 stainless steel-zirconium alloys. *Metall. Mater. Trans. A.* **27A**, 2151–2159 (1996).
13. McDeavitt, S. M., Billings, G. W. & Indacochea, J. E. High temperature interaction behavior at liquid metal-ceramic interfaces. *J. Mater. Eng. Perform.* **11**, 392–401 (2002).
14. Bauer, T. H. et al. Corrosion and constituent release from a metal waste form. *Proceedings of the International High-Level Radioactive Waste Management Conference*. Las Vegas, Nevada. CD-ROM. Session E-3 Source Term-I: General Modeling Topics. La Grange Park, Illinois: American Nuclear Society (2001).
15. Ebert, W. L., Lewis, M. A., Barber, T. L. & Johnson, S. G. Accounting for EBR-II metallic waste form degradation in TSPA. Scientific Basis for Nuclear Waste Management XXVI, Symposium. *Mater. Res. Soc. Symp. Proc.* R. J. Finch, and D. B. Bullen, eds., Boston, Massachusetts. Vol. 757, pp. 71–80 (2002).
16. Johnson, S. G. et al. Leaching characteristics of the metal waste form from the electrometallurgical treatment process: product consistency testing. Scientific Basis for Nuclear Waste Management XXIII, Symposium. *Mater. Res. Soc. Symp. Proc.* R. W. Smith, and D. W. Shoesmith, eds., Boston, Massachusetts. Vol. 608, pp. 589–594 (1999).
17. Johnson, S. G., Noy, M., DiSanto, T. & Barber, T. L. Release of neptunium, plutonium, uranium, and technetium from the metallic waste from the electrometallurgical treatment process. Scientific Basis for Nuclear Waste Management XXV, Symposium. *Mater. Res. Soc. Symp. Proc.* B. P. McGrail, and G. A. Cragnolino, eds, Boston, Massachusetts. Vol. 713, pp. 705–711 (2001).
18. Westphal, B. R. et al. Characterization of irradiated metal waste from the pyrometallurgical treatment of used EBR-II fuel. *Metall. Mater. Trans. A.* **46**, 83–92 (2015).
19. Ebert, W. L. & Gattu, V.K. Production and initial testing of RAW-6 materials. *DOE NE Report*. Argonne National Laboratory. FCRD-MRWFD-2016-000350 (2016).
20. Han, S. et al. The corrosion properties of Zr-Cr-NM alloy metallic waste form for long-term disposal. *J. Nucl. Fuel Cycl. Wast. Tech.* **15**, 125–133 (2017).
21. Gattu, V. K. Role of alloying elements in the electrochemical corrosion behavior of multiphase alloys. *Dr. Diss.* University of Illinois at Chicago (2017).
22. Birbilis, N., Choudhary, S., Scully, J. R. & Taheri, M. L. A perspective on corrosion of multi-principal element alloys. *Npj Mater. Degrad.* **5**, 1–8 (2021).
23. Bagchi, A. C., Prasad, G. J., Khan, K. B. & Singh, R. P. Physical metallurgy studies of Zr-rich U-Zr alloys. *J. Mater. Sci. Eng.* **2**, 1–6 (2013).
24. Malik, A. U., Mayan Kutty, P. C., Siddiqi, NadeemA., Andijani, IsmaeelN. & Ahmed., Shahreer The influence of pH and chloride concentration on the corrosion behaviour of AISI 316L steel in aqueous solutions. *Corros. Sci.* **33**, 1809–1827 (1992).
25. Gattu, V. K., Ebert, W. L., Indacochea, J. E. & Frank, S. M. Electrochemical corrosion of a multiphase alloy/oxide composite nuclear waste form. *Corros. Sci.* **184**, 109358 (2021).
26. Rahman, T., Ebert, W. L. & Indacochea, J. E. Effect of molybdenum additions on the microstructures and corrosion behaviours of 316L stainless steel-based alloys. *Corros. Eng. Sci. Tech.* **53**, 1–8 (2018).
27. Gattu, V. K., Olson, L., Ebert, W. L. & Indacochea, J. E. Corrosion resistance by design. *Int. Corros. Conf. Proc.* NACE International. Paper No. 15183 (2020).
28. Gattu, V. K., Ebert, W. L., Tehrani, N. & Indacochea, J. E. Electrochemical measurements of steel corrosion for modeling H_2 generation. *Int. Corros. Conf. Proc.* NACE International. Paper No. 11370 (2018).
29. Stern, M. & Wissenberg, H. The electrochemical behavior and passivity of titanium. *J. Electrochem. Soc.* **106**, 759 (1959).
30. Jerden, J. L. Jr., Frey, K. & Ebert, W. L. A multiphase mixed potential model for spent fuel dissolution. *J. Nucl. Mater.* **462**, 135–146 (2015).
31. McCafferty, E. Introduction to corrosion science (Springer Science & Business Media, NY, 2010).
32. Frank, S. M., Hahn, P. A., Ebert, W. L. & Olson, L. Test alloy fabrication and oxide addition studies. *DOE NE Report*. FCRD-SWF-2012-000234 (2012).

AUTHOR CONTRIBUTIONS

V.K.G., W.L.E., J.E.I., T.A.C., and J.A.F. designed the research, performed the experiments and analyzed the data. V.K.G., W.L.E., and J.E.I. prepared the main text, advised on the experiments and aided in manuscript editing. V.K.G. aided in experiment development and performance. All authors reviewed and approved the manuscript.

COMPETING INTERESTS

The authors declare no competing interests.

ADDITIONAL INFORMATION

Correspondence and requests for materials should be addressed to Vineeth Kumar Gattu.

Reprints and permission information is available at http://www.nature.com/reprints

Publisher's note Springer Nature remains neutral with regard to jurisdictional claims in published maps and institutional affiliations.